



ELSEVIER

Contents lists available at ScienceDirect

Earth and Planetary Science Letters

journal homepage: www.elsevier.com/locate/epsl

Arrest of the Mw 6.8 January 24, 2020 Elazığ (Turkey) earthquake by shallow fault creep

Ziyadin Cakir^{a,*}, Uğur Doğan^b, Ahmet M. Akoğlu^a, Semih Ergintav^c, Seda Özarpacı^b, Alpay Özdemir^b, Tohid Nozadkhalil^a, Nurdan Çakır^a, Cengiz Zabcı^a, M. Hilmi Erkoç^b, Mehran Basmenji^a, Mehmet Köküm^d, Roger Bilham^e

^a Istanbul Technical University, Department of Geological Engineering, Istanbul, Turkey

^b Yildiz Technical University, Department of Geodesy, Istanbul, Turkey

^c Bogazici University, Kandilli Observatory and Earthquake Research Institute, Department of Geodesy, Istanbul, Turkey

^d Firat University, Department of Geological Engineering, Elazığ, Turkey

^e University of Colorado, CIRES & Geological Sciences, Colorado, USA

ARTICLE INFO

Article history:

Received 21 April 2022

Received in revised form 12 February 2023

Accepted 26 February 2023

Available online xxxx

Editor: J.P. Avouac

Keywords:

rupture arrest

creep

afterslip

earthquake cycle

ABSTRACT

It has long been conjectured that creeping sections of strike slip faults arrest or subdue earthquake rupture, partly because of their reduced slip potential and partly because of their velocity-strengthening frictional properties. However, no instrumentally recorded large earthquake ($M_w \geq 6.8$) on any well instrumented continental strike-slip fault has thus far occurred that has clearly been arrested at a region of fault creep, rendering it difficult to identify experimentally the parameters that control rupture arrest. Nearfield GPS, InSAR and creepmeter data from the 2020 Elazığ (Turkey) earthquake reveal not only how rupture propagation of a large earthquake is hindered by shallow creep reducing the earthquake size, but also provide important quantitative insights into the late interseismic, coseismic and post seismic behavior of a creeping fault, which has important implications for evaluating hazard potential of a major earthquake on a creeping fault, such as has been forecast for the Hayward fault in California.

© 2023 Elsevier B.V. All rights reserved.

1. Introduction

Ruptures of major continental strike-slip earthquakes generally nucleate near the base of the seismogenic crust and propagate upward and laterally until they are arrested by mechanical or geometrical barriers in the form of step-overs or bends (Aki, 1979). In general, The more segments that rupture, the greater the size of the earthquake and the consequential damage (Nissen et al., 2016). It has long been thought that creeping sections of faults can act as barriers to earthquake rupture propagation partly because of their velocity strengthening frictional behavior (Thatcher, 1975; Lindh and Boore, 1981; Marone et al., 1991), and partly because of their reduced slip potential (Bürgmann et al., 2000). Striking examples are the 1857 Fort Tejon and 1906 San Francisco earthquakes that appear to have nucleated or terminated at the ends of the central creeping segment of the San Andreas fault in California (Sieh, 1978; Thatcher, 1975). However, the absence of large earthquakes on well monitored creeping strike slip faults during

the instrumental period makes it difficult to identify experimentally the parameters that control rupture arrest, and evaluate the hazard potential of a major earthquake on creeping faults. Reasons for this are that creeping faults with a well constrained geodetic history of hybrid creep and seismic rupture are relatively rare and no major earthquakes have occurred near these locations in the past several decades (Harris, 2017). To determine the future seismic behavior of these regions, considerable theoretical ingenuity has been expended in simulating the influence of fault creep in arresting or subduing a rupture. However, though these studies have provided insights into rupture propagation into creep dominated fault regimes, the constraints derived from these theoretical models depend on trade-offs in a range of numerical values of physical parameters used in the simulations (Kaneko et al., 2010; Noda and Lapusta, 2013; Avouac, 2015; Harris, 2017). Detailed field observations and instrumental measurements on creeping faults and contiguous major earthquakes provide crucial constraints on these input parameters, not only for effective seismic hazard mitigation but also for a better understanding of the nucleation and arrest of earthquakes (Bürgmann et al., 2000; Hough and Martin, 2015; Avouac, 2015; Chen and Bürgmann, 2017). Here we analyze GPS, InSAR and creepmeter data from the January 24, 2020

* Corresponding author.

E-mail address: ziyadin.cakir@itu.edu.tr (Z. Cakir).

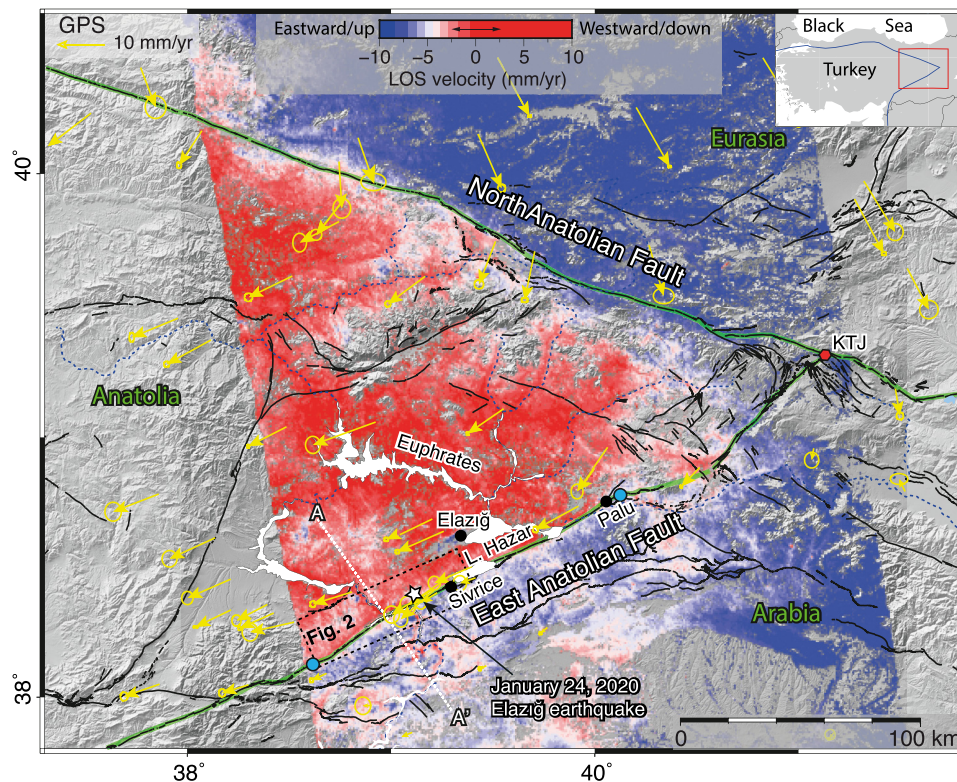


Fig. 1. Tectonic map of Eastern Turkey with active faults (black lines) (Emre et al., 2018), depicting the configuration of Anatolian, Arabian and Eurasian plates that meet at the Karlıova Triple Junction (KTJ) and their relative motions deduced from GPS (yellow arrows with 95% confidence ellipses in Arabian reference frame (Reilinger et al., 2006) and InSAR observations (color coded mean line-of-sight velocity field on Sentinel-1 ascending track 43) on a shaded elevation image from Shuttle Radar Topographic Mission 90-m posting digital elevation data (Farr and Kobrick, 2000). White star indicates the epicenter of the January 24, 2020 Mw 6.8 Elazığ earthquake. Blue circles mark the edges of the creeping section along the East Anatolian Fault.

Mw 6.8 Elazığ earthquake on the East Anatolian Fault (EAF) in eastern Turkey, which provides important quantitative insights into the behavior of a creeping fault during the earthquake cycle (Fig. 1).

2. January 24, 2020 Mw 6.8 Elazığ earthquake

The 2020 Elazığ earthquake ruptured the central section of the East Anatolian Fault (EAF), a ~600-km long major left-lateral strike-slip fault in Eastern Turkey that accommodates a relative motion of ~10 mm/yr between the Arabian and Eurasian plates (Reilinger et al., 2006) (Fig. 1). Together with its conjugate, the North Anatolian Fault, the EAF accommodates the westward escape of the Anatolian plate from the continental collision between the Arabian and Eurasian plates that commenced during the Late Miocene (~11 ma) along the Bitlis-Zagros suture in southeastern Turkey and Iran (Şengör et al., 1985). Based on geological and morphotectonic observations, the total offset along the EAF has been estimated to be around 25 km (Duman and Emre, 2013). Unlike the NAF that exhibited a remarkable westward migration of large earthquakes during the 20th century, the EAF had been mostly quiet since the 19th century (Duman and Emre, 2013).

The earthquake broke almost half of the Pütürge seismic gap along the EAF (Duman and Emre, 2013), causing extensive damage particularly in the city of Elazığ and giving rise to 41 fatalities and hundreds of injuries due to the collapse of poorly constructed buildings. Earthquake scaling laws (Wells and Coppersmith, 1994) predict that earthquakes of this magnitude on continental strike slip faults can be expected to produce a ~30 km-long surface rupture. It was with some surprise then, no surface rupture was reported although postseismic investigations yielded significant evidence for widespread fissures, landslides and fractures related to lateral spreading along the historical fault trace (Tatar et al., 2020).

The absence of an extensive coseismic surface rupture was subsequently confirmed by interferometric synthetic aperture radar (InSAR) observations based on European Union's Sentinel 1A/B satellites that imaged the earthquake area 3 days after the mainshock (Pousse-Beltran et al., 2020; Ragon et al., 2021; Taymaz et al., 2021; Konca et al., 2021). InSAR and seismological observations reveal that a ~40-km-long subsurface segment of the EAF fault between Sivrice and Doğanyol ruptured from a nucleation depth of around 12 km propagating upwards and mostly south-westward along the fault, terminating a few kilometers below the surface (Taymaz et al., 2021; Pousse-Beltran et al., 2020; Ragon et al., 2021). The subsurface arrest of the rupture apparently resulted in a slip deficit of the order of 1 m on the shallow fault. Previous studies have invoked various reasons for this slip deficit: immaturity of the fault (Taymaz et al., 2021; Pousse-Beltran et al., 2020), fault geometry (restraining bend) (Tatar et al., 2020), presence of metamorphic rocks (Tatar et al., 2020), artifacts in modeling (Ragon et al., 2021), inefficient dynamic stresses (Galović et al., 2020), and inferred surface creep (Chen et al., 2020; Konca et al., 2021). We show here that this surface segment was the locus of aseismic slip in previous decades, that rapid afterslip is currently with a decaying rate following the earthquake.

3. Surface deformation due to the earthquake cycle along the Pütürge Fault

3.1. Geodetic data sets and processing

We use the European Space Agency's Envisat and Sentinel-1, and Japanese Space Agency's ALOS-2 radar satellite data to calculate the surface deformation during the earthquake cycle in the study region. The number of images and the time spanned are

given in Supplementary Table 1. Envisat raw data are focused to single look complex images using ROI_PAC (Rosen et al., 2000), from which interferograms are calculated using the Doris InSAR processing software (Kampes and Usai, 1999). Sentinel-1 Interferometric Wide (IW) swath data are processed using the Generic Mapping Tools Synthetic Aperture Radar open source InSAR processing tools (Sandwell et al., 2011). ALOS-2 data are processed using the InSAR Scientific Computing Environment (ISCE) software (Rosen et al., 2015; Liang and Fielding, 2017). Effects of topography in all the interferograms, except the coseismic ones, are removed using the Shuttle Radar Topography Mission (SRTM) 1-arcsec posting digital elevation model. A 12-m posting TerraSAR- X DEM is used to simulate the topographic phase in the coseismic interferograms. Unwrapping errors and areas with deformation due to gravitational mass movements along slopes are also corrected/removed manually in the coseismic interferograms. In addition to the 20 km span of the EAF that is covered with water (due to the Euphrates River), there were additional incoherent areas near the fault zone. These too are removed using a coherence threshold of 0.2. A trend is then removed from the unwrapped coseismic interferograms. The final unwrapped data are subsampled using the quadtree algorithm (Jónsson et al., 2002).

InSAR time series for the interseismic and postseismic periods are calculated with a single master network of interferograms using the software package StaMPS that allows the selection of persistent scatterers using both amplitude and phase information (Hooper et al., 2012). The TRAIN Toolbox (Bekaert et al., 2015) is used to correct atmospheric effects in InSAR measurements with ERA Interim data (Dee et al., 2011) for interseismic InSAR time series, and a power law function for the postseismic time series.

Interseismic displacements prior to the earthquake are mapped using Envisat data acquired between 2003 and 2010 on both descending and ascending tracks (Supplementary Fig. 1). We use Sentinel-1 data for mapping the interseismic displacements between 2014 and 2019, and postseismic displacements between 2020 and 2022 on two ascending and one descending tracks (Supplementary Figs. 2-4). Mean LOS interseismic velocities calculated from InSAR time series in the descending and ascending tracks are decomposed into vertical and horizontal (east-west) components (Funning et al., 2005). The latter is further projected on to the fault strike assuming that the east-west horizontal motions are merely due to left-lateral motions due to relative plate motions across the EAF (Supplementary Fig. 5). Figs. 2a and 2b show mean fault parallel Envisat and Sentinel velocity fields obtained by stacking fault parallel velocity fields decomposed from different combinations of ascending and descending tracks.

Survey and continuous GPS (Fig. 1) data are processed using GAMIT/GLOBK software (Herring et al., 2010) with the final ephemerides of IGS (International GNSS Service, <http://igs.csb.jpl.nasa.gov>) products between 2010 and 2021 for continuous GPS (cGPS) sites between 2015 and 2021 in ITRF2014 (International Terrestrial Reference Frame) for survey GPS (sGPS) sites. While the nearest cGPS station is located 30 km to the north in Elazığ city, five sGPS sites are present within a few km from the fault in the earthquake area (Figs. 1, 2c). Seven campaigns before the earthquake (biannually with the exception of 2018) and 3 survey campaigns following the event were carried out in sessions of at least 10 hours using dual-frequency GPS receivers and geodetic antennas. The cGPS sites were reoccupied a day after the earthquake in order to estimate coseismic offsets with negligible postseismic deformation using a linear extrapolation of pre-earthquake data to the day of the earthquake (Fig. 2; Supplementary Fig. 6; Reilinger et al., 2006).

We installed a creepmeter 11 days after the earthquake on the fault near the epicenter (38.388°E, 39.187°N) where we observed en-echelon fractures on the frozen snow a few days after the main

shock (Fig. 2d). The creepmeter is 16-m long and was installed at 30° to the fault resulting in a fault-normal sampling width of 8 m. Nearby en-echelon cracks seen in the adjoining road surface, and briefly in the crust of recent snow, were approximately 2-m wide and were estimated to have been caused by ~3 cm of sinistral shear.

3.2. Modeling surface deformation

We model the inter-, co- and post-seismic deformation captured by InSAR (in line-of-sight) and GPS (in horizontal) using Poly3D, a 3D-boundary element method that uses triangular dislocations in a linear elastic and homogeneous half-space (Thomas, 1993). Inversions are carried out with Poly3Dinv software that uses a damped least square minimization and a scale-dependent umbrella smoothing operator to avoid any nonphysical oscillatory slip distribution (Maerten et al., 2005). Using triangular elements allows one to generate a more realistic 3D fault surface and to avoid the possibility of gaps that can be encountered in the middle of the earthquake rupture due to a ~10° change in the fault strike when rectangular dislocations are used. In order to find an optimum fault dip, a Monte Carlo based analysis with simulated annealing nonlinear search scheme is used with a single rectangular fault (Sudhaus and Jónsson, 2009). We then construct a triangular mesh of 90 km long that follows the surface trace of the EAF from surface down to 19 km of depth with a uniform dip value of 77° based on the results of the Monte Carlo based analysis, in agreement with the seismological focal mechanism solutions (Supplementary Table 2; Supplementary Fig. 7). Before modeling the interseismic creep and postseismic afterslip on the triangulated fault surface, interseismic deformation is inverted and removed from the velocity fields using a deep lithospheric scale vertical fault below the modeled fault (Supplementary Figs. 8-10). Although background seismicity, InSAR data, mainshock and aftershocks all suggest a dipping fault along this section of the EAF (Pousse-Beltran et al., 2020; Konca et al., 2021, Supplementary Table 2, Fig. 2e), we use a vertical shear zone below the fault. This is because a lithospheric scale dipping fault gives rise to an asymmetry in the velocity fields across the fault, which is not observed neither in the GPS nor in the InSAR interseismic velocity fields. It is very likely that fault steepens downwards below the lower crust. However, for the sake of simplicity, a single vertical fault 19 km below the fault trace is used.

In order to evaluate the uncertainty of slip inverted for inter-, co- and post-seismic phases, spatially correlated noise based on data co-variance is generated and added to the InSAR data sets and then inverted 500 times (e.g., Funning et al., 2005; Sudhaus and Jónsson, 2009). Standard deviations are then calculated on each triangular patch and then slip with high standard deviations (>65% of the inverted slip) is filtered out from final slip distributions (Supplementary Fig. 11).

We also used profiles of fault-parallel horizontal InSAR velocities to calculate the rate of creep and afterslip along the surface trace of the fault. 6-km long fault perpendicular profiles (3 km on each side of the fault) are extracted from these maps at about every 1.5 km (Supplementary Fig. 4i). Considering the density of the PS points in the velocity maps, data sampling width across the profiles is chosen to be 2 km for Envisat and 0.4 km for the Sentinel velocity maps. Data points within 0.5 km from the fault are discarded. We calculate creep rate and amount of afterslip along the fault by fitting a linear trend to fault parallel horizontal displacements and calculating the offset at the fault trace as the rate of creep or afterslip (Supplementary Fig. 12). Error bars given are based on 1-standard deviation of the root-mean-square residuals obtained following the linear regression.

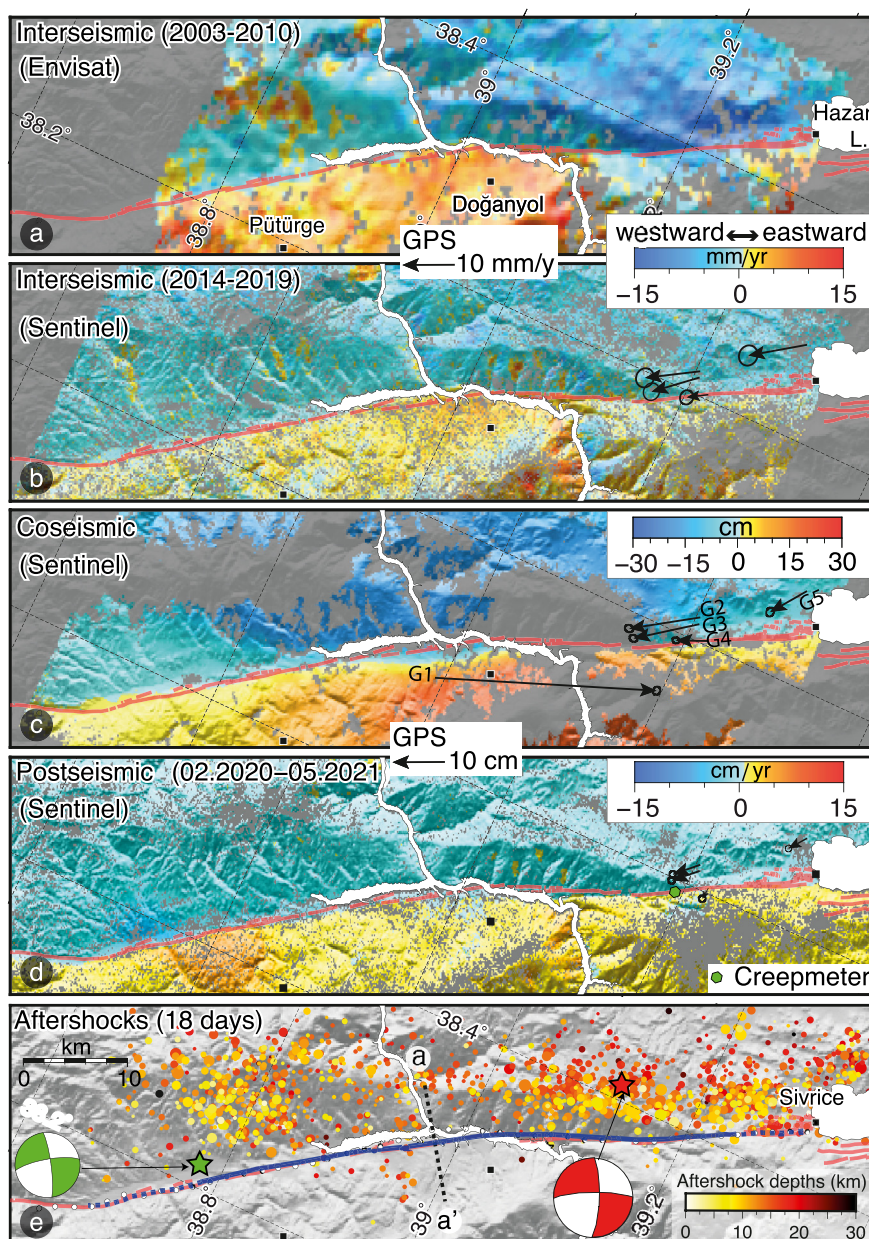


Fig. 2. InSAR and GPS measurements during the earthquake cycle, and distribution of the first 18 days of aftershocks. Color coded images shaded with the SRTM data are fault parallel (N56°E) InSAR velocities and offsets during the interseismic (a, b), coseismic (c) and postseismic (d) periods. (e) Distribution of aftershocks (fill color is based on focal depths) during an 18-day period following the January 24, 2020 Mw 6.8 Elazığ earthquake (Melgar et al., 2020). Blue line indicates projection of the rupture to the surface based on the extent of the coseismic slip higher than 20 cm at depth. Red and green beach balls show the focal mechanisms of the mainshock and the largest aftershock (Mw 5.6 August 4, 2020), respectively. Note the depth distribution of aftershocks and their location being overwhelmingly on the northern side of the fault indicate a significant northward dip. Dashed line a-a' shows the location of the profile given in Fig. 3. Red lines are active faults.

3.3. Interseismic deformation

As seen in Figs. 2a and 2b, the sharp change in the mean fault parallel interseismic velocity field across the Pütürge fault is clear evidence for surface creep, which appears as a step in the velocity field across the fault as observed in fault perpendicular profiles of A-A' in Fig. 3 (see Supplementary Fig. 13 for other profiles). The presence of surface creep is also clearly manifest in GPS velocities available towards the eastern end of the earthquake rupture near Lake Hazar (Figs. 2b, 3). The Paleozoic metamorphic rocks made of up mostly mica-schist, through which the Pütürge segment runs, appear to be what facilitates fault creep as they provide the velocity-strengthening, weak phyllosilicate minerals in the fault gouge necessary for creep (Carpenter et al., 2011) (Supplementary

Fig. 14). We note that this shallow creep that extends ~75 km further to the east along the fault (Fig. 1) was undetected in previous InSAR studies (Cavalié and Jónsson, 2014; Bletery et al., 2020), most likely due to the different MT-InSAR technique they used with over multi-looking of SAR images, and subsequent coarse spatial sampling in order to increase the signal to noise ratio. The Envisat and Sentinel-1 velocity fields are in good agreement and show that the Pütürge segment had been creeping at rates varying from a few mm/yr up to the far field plate velocity of 1 cm/yr at least since 2003 until the January 2020 rupture (Figs. 4a, b). While surface creep is fairly shallow and confined mostly to the uppermost 3-4 km of the crust on the western side of the fault, it penetrates much deeper depths to the east where the fault appears to be locked at shallow depths. The depth of the hypocenter sug-

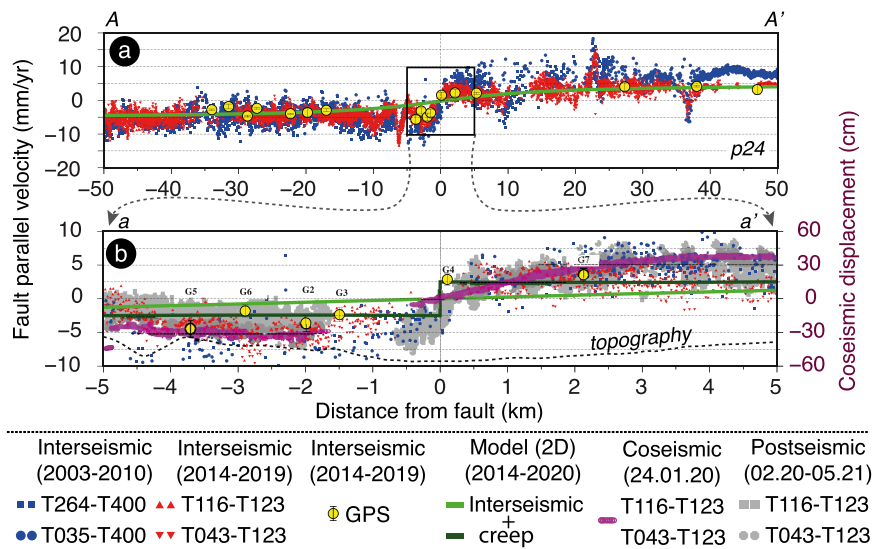


Fig. 3. Profiles of fault-parallel interseismic InSAR and GPS velocities (with 1σ uncertainties) and coseismic and postseismic offsets across the Puturge segment. (a) Interseismic velocities along profile A-A' shown in Fig. 1. Envisat (blue dots) and Sentinel-1 (red dots) InSAR data and GPS measurements (yellow circles with 1 uncertainties) are in excellent agreement and reveal surface creep as a step at the fault. Paired numbers in the legend (e.g., T264-T400) show track numbers of satellites used to calculate horizontal velocities and displacements (Supplementary Figs. 1, 2). (b) Close-up view of profile A-A' in the near field (see Fig. 2e for its location) together with coseismic and postseismic offsets and interseismic models with and without creep. Note that the rupture does not reach the surface since the coseismic displacements (purple dots) show no discontinuity across the fault. However, following the main shock the fault starts creeping as afterslip (gray dots).

gests that the rupture probably nucleated within the ductile-brittle transition zone at depth.

3.4. Coseismic deformation

Coseismic surface deformation of the main shock was captured by Sentinel-1 and ALOS-2 SAR satellites and sparsely distributed GPS stations (Fig. 2c; Supplementary Fig. 4). The pattern and continuity of coseismic deformation in interferograms (Supplementary Fig. 4) and displacement profiles (e.g. Fig. 3) across the fault along most of its trace imply that the surface rupture hardly reaches to surface. This observation is consistent with our field observations and GPS measurements west of Lake Hazar where the coseismic displacement few hundred meters to the fault (i.e. G4 and G5 in Fig. 2c) is significantly smaller than those just 2-2.5 km to the north, implying relatively much higher coseismic slip below the surface (Fig. 2c). The slip distribution obtained by triangular dislocation modeling shows an elongated elliptical pattern with three lobes of high slip or asperities below the shallow creeping sections of the fault, in good agreement with previously inferred slip distributions (Taymaz et al., 2021; Pousse-Beltran et al., 2020; Ragon et al., 2021; Gallovič et al., 2020; Melgar et al., 2020) (Fig. 4c). Coseismic slip peaks to 1.9 m at depths of ~ 4 km above the hypocenter with only a few cm of slip at the surface near the epicenter (Figs. 4c, d). The point where the earthquake nucleates on the subsurface fault is located at the edge of the high slip lobe, again in good agreement with slip distribution deduced from tele-seismic body-wave finite-fault inversions (Gallovič et al., 2020; Taymaz et al., 2021), supporting the hypothesis that the nucleation point is often located in regions of low coseismic slip (Reilinger et al., 2006; Floyd et al., 2016). Although the peak slip occurs at shallow depths (4-5 km), coseismic slip decreases rapidly towards the surface from nearly 2 m to near zero at depths of 1-1.5 km, leaving the shallowest segment of the fault with apparently no significant slip. In the following section we discuss below the implications of en-echelon surface cracks and subsequent creep on the surface fault near the epicenter. The western end of the rupture appears also to be associated with aseismic near-surface creep. (Fig. 4a).

3.5. Postseismic deformation

Large earthquakes, particularly those on strike slip faults, are often followed by afterslip at shallow depths (Bilham, 1989; Cakir et al., 2012; Floyd et al., 2016; Harris, 2017; Nevitt et al., 2020). Previous InSAR studies report a few cm of afterslip following this earthquake (Pousse-Beltran et al., 2020; Taymaz et al., 2021; Gallovič et al., 2020), but claim that afterslip ceased after a few weeks. In order to better estimate the spatiotemporal characteristics of the afterslip, we have calculated InSAR time series using Sentinel-1 data spanning a time interval of 16 months following the main shock. We use not only a single track, but all the available tracks of the Sentinel-1 satellite that cover the earthquake area from 3 different look angles (Supplementary Fig. 3). Fig. 2d shows the mean velocity map calculated from mean decomposed horizontal velocities using the same procedure applied to the interseismic InSAR time series describe above. Afterslip, like interseismic creep, is manifest as an abrupt reversal in the direction of horizontal motions within a distance of ± 150 m across the fault. As seen in Figs. 4d and 4e, and noticed previously (Taymaz et al., 2021), afterslip is not confined to the broken section of the fault, but extends well beyond the rupture tips, reaching up to 15 cm/yr of slip toward the edges of the earthquake rupture. Modeling of postseismic InSAR data indicates that afterslip on the fault surface is taking place within the shallow slip zone and around the coseismically ruptured subsurface at depth (Fig. 4d). Note that most of the large-amplitude afterslip to the west of the coseismic slip area is in fact coseismic slip of the largest aftershock (Mw 5.6) that took place on August 4, 2022 (see Supplementary Fig. 15).

Checker box tests and uncertainty analysis using inversions of InSAR data with spatially correlated synthetic noise indicate that most slip down to about 3-4 km of depth is resolvable (Supplementary Fig. 16). Although, the uncertainties of inverted coseismic slip between 39.00E and 39.15E are relatively high due to the absence of coseismic InSAR data in the nearfield to the north of the fault where coherences of interferograms are low, interseismic and postseismic slips at shallow depths have relatively lower uncertainties all along the fault due to the presence of abundant nearfield InSAR data points (Supplementary Fig. 4).

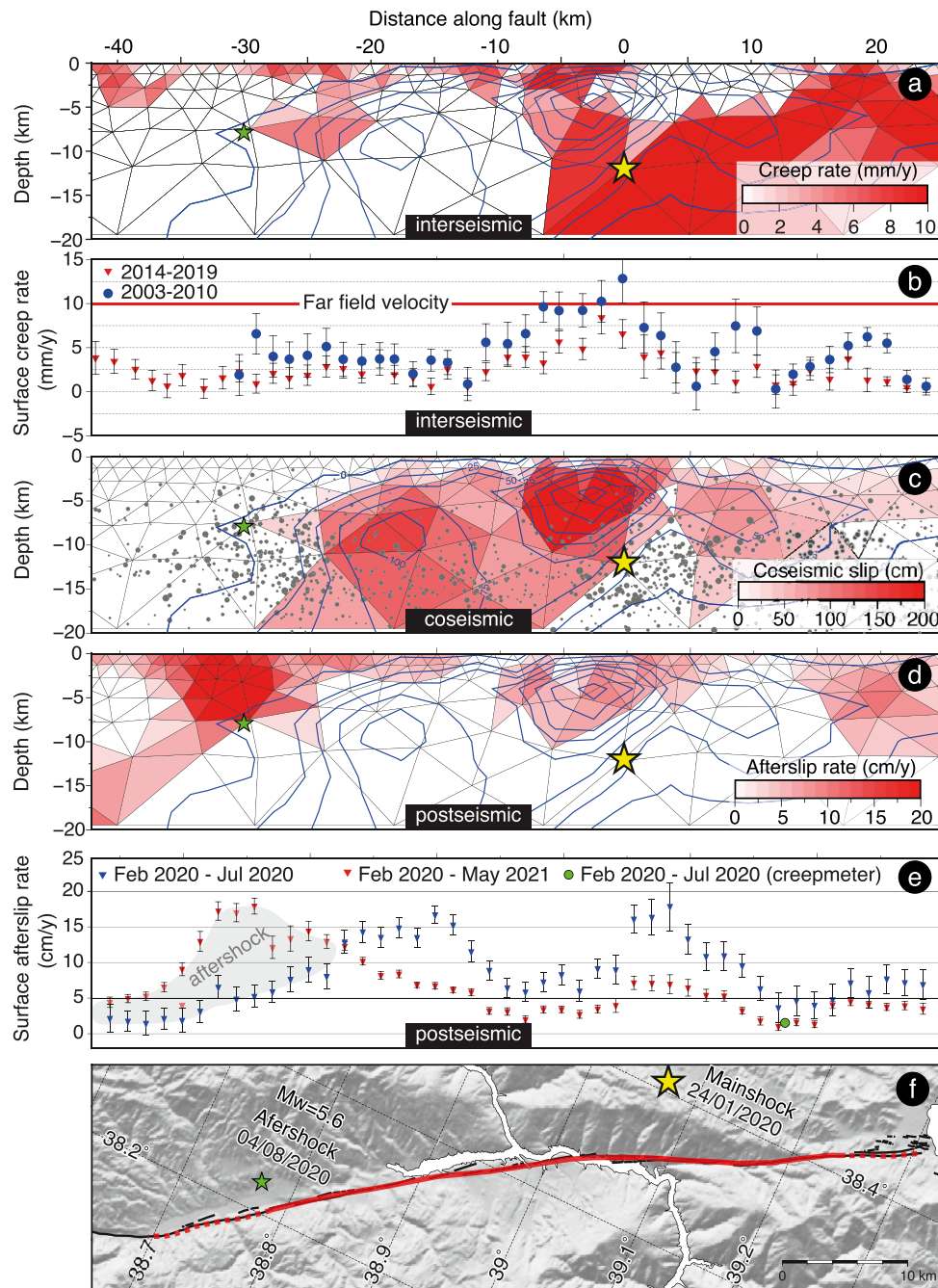


Fig. 4. Spatiotemporal evolution of slip on the Puturge segment during the earthquake cycle. (a) Interseismic slip distribution based on Envisat and Sentinel data (Figs. 2a, b), showing shallow and deep creep together with the hypocenters of the main shock (yellow star) and the largest (Mw 5.6) aftershock (green star) in August 4, 2020. Blue lines are contours of coseismic slip in (c). (b) Surface creep rate along the fault inferred from Envisat (blue circles) and Sentinel-1 (inverted triangles) data. c. Distribution of coseismic slip and the first 18 days of aftershocks (gray circles). Note that the aftershocks surround the region of coseismic slip which barely reaches to the surface. (d) Distribution of afterslip during the first 16 months of the postseismic period. The August 4, 2020 aftershock (green star) coincides with the western tip of the coseismic rupture. (e) Postseismic afterslip at the surface before and after the August 4, 2020 aftershock from InSAR (inverted triangles) and creepmeter (green circle) measurements. (f) Projection of the rupture to the surface (red line) based on the extent of the coseismic slip at depth, and the extent of afterslip observed at the surface (dashed lines). Note that the slip distributions at different periods spatially complement each other; while the shallow slip deficit is filled by interseismic creep and postseismic afterslip, deeper slip deficit is filled by coseismic slip.

Contrary to the previous claims of rapid decay in afterslip, the creepmeter measurements show that afterslip continued during at least ~2.5 years following the earthquake, reaching 12 cm of cumulative slip. It will likely continue for some time as its rate of ~16 mm/yr over the last year is still higher than the far field plate velocity (~10 mm/yr) (Fig. 5a). The first 18 days of afterslip data from the creepmeter are fit to an exponential decay with a

time constant of 16.7 days, which suggests that surface slip started 4.5 ± 2 days after the main shock (Supplementary Fig. 17). A double exponential decay curve can be fit to segments of the entire data with the form:

$$Slip(t) = y_0 + A1 \exp[-(t - t_0)/\tau_1] + A2 \exp[-(t - t_0)/\tau_2] \text{ mm} \quad (1)$$

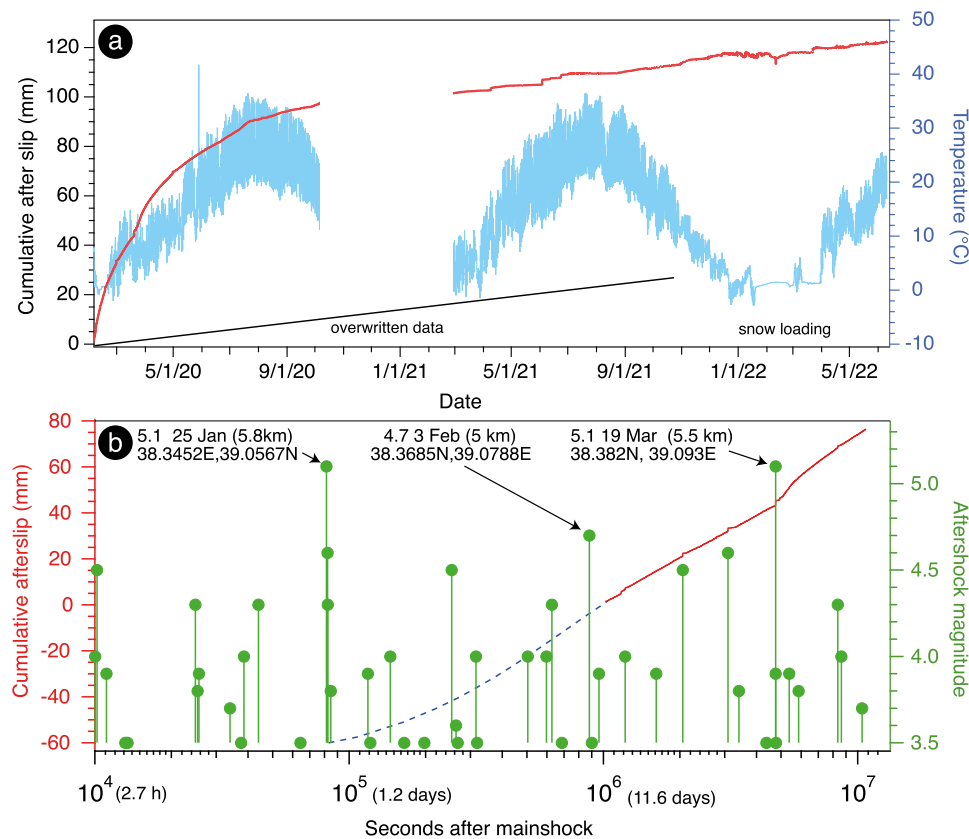


Fig. 5. Results of creepmeter measurements. (a) Evolution of afterslip recorded by creepmeter in the 2.5 years following the earthquake. The first year of data is characterized by exponentially decreasing slip with a time constant ~ 30 days. Data were lost during the winter of 2021 after which a linear creep rate of 16 mm/yr is observed. (b) Log/linear plot of aftershocks and afterslip from 11 days to 4 months after the mainshock. Blue dashed line in (b) is an extrapolated double-exponential fit to pre-March 19 creep data. It implies that several hours after the mainshock, 60 mm of coseismic slip had been established at, or close to, the surface at this location (less than 5 km east of the epicenter).

where A is the amplitude of slip at time t , y_0 is the offset at $t = 0$ and τ is a time constant associated with the rate of decay.

Prior to a $M_w=5.1$, 5.5-km-deep aftershock on 19 March, a curve with a decay time constant of 27 days fits the data to within ~ 1 mm accuracy (Fig. 5b). The 19 March aftershock was associated with sufficient subsurface displacement to incrementally renew afterslip. A second exponential with $\tau = 32$ days can be fit with similar precision to post 20-March data. The similarity of these time constants suggests that similar rheology for mainshock and aftershock moderates the manifestation of surface slip.

A quantitative estimate of slip prior to the installation of the creepmeter can be derived by extrapolating surface slip measured by the creepmeter back to a time a few hours after the mainshock (Fig. 5b). This shows that roughly 60 mm of slip preceded the installation of the creepmeter, a value that is approximately double the 30 mm estimated from the apparent slip estimated from the en-echelon cracks crossing the nearby road, but consistent with the uncertainties attending this estimate. In view of the probable perturbing effects of early aftershocks with similar magnitudes and distances to the 19 March aftershock, uncertainties in this extrapolation almost certainly exist. However, the finding indicates that approximately 6 cm of shallow slip occurred within a few hours to a day of the mainshock. This slip was registered as en-echelon surface cracks indicating that the causal dislocation terminated in the subsurface. The thickness of the surface layer that impeded through-going surface rupture is conjectural, but it may initially have exceeded 30 m according the results of Parker et al. (2021), and presumably shallowed in the following weeks and months (Nevitt et al., 2020).

4. Spatiotemporal evolution of slip over the earthquake cycle

Slip behavior of the Pütürge segment of the East Anatolian fault and its spatiotemporal characteristics provide insights to our understanding of the interplay between aseismic and seismic fault slip over the earthquake cycle, rupture mechanics and earthquake physics (Avouac, 2015). As noted by previous studies, a striking coseismic slip deficit is present along the uppermost section of the fault (Fig. 4). This shallow slip deficit is the locus of interseismic creep and postseismic afterslip that display a spatially complementary pattern of surface slip along the fault with afterslip being minimum near the peak interseismic creep rate. We note that the shallow slip deficit is also partially released by the rupture zone of the aforementioned $M_w 5.6$ August 4, 2020 aftershock, where interseismic creep was negligible. Taking into account the slip rate of the fault, interseismic creep rate and amount of afterslip, we conclude that additional afterslip or similar shallow earthquakes are required to close the deficit in the slip budget at shallow depths where the interseismic creep rate was observed to be low. The spatial correlation between coseismic slip and aftershocks is also quite remarkable as the latter surrounds the patches of coseismic slip, except at superficial depths, suggesting that aftershocks are driven by deep afterslip (Hsu et al., 2006), which extends well beyond the rupture tips along the strike of the fault (Figs. 4d, e; Supplementary Fig. 3). Anticorrelation between the pre-seismic creep rate and the cumulative afterslip along the fault at surface implies that the shallow coseismic slip deficit is compensated by aseismic slip during the interseismic and postseismic phases of the earthquake cycle (Fig. 4).

5. Arrest of rupture propagation

Observations and modeling of the geodetic data sets imply that rupture propagation was suppressed abruptly towards the surface where it encountered the shallow creeping section, resulting in ~8% reduction in seismic moment release (equivalent to an earthquake of magnitude 6.0), considering 1-m slip deficit along a 30-km long, 1.5-km wide uppermost section of the fault. The sudden arrest at shallow depths requires a significantly higher a-b value of the rate and state friction law in this shallow velocity strengthening creeping section (Marone et al., 1991). This is somewhat similar to what was observed on the southern half of the Mw 6.0, 2004 Parkfield (Johanson et al., 2006; Brooks et al., 2017) and the Mw 6.6, 1987 Superstition Hill (Marone et al., 1991), where shallow creep prevailed. In the case of the Superstition Hills fault, pre-seismic creep was insignificant (<1 mm/yr). In the following hours and weeks in both earthquakes subsurface rupture propagated upward into the velocity strengthening region releasing part of the shallow slip deficit (Marone et al., 1991; Bilham, 2005). Although slip on the creeping San Andreas fault in the 2004 Parkfield Mw 6.0 earthquake was likely hindered by shallow creep, an earthquake of this size is not expected to reach to the surface, considering its peak slip of 40 cm located at a depth around 6 km (Johanson et al., 2006). A similar rupture arrest was also observed following the 2003 Mw 6.8 Chengkung Earthquake on the creeping Longitudinal Valley Fault, Taiwan (Thomas et al., 2014). However, this event is associated with a reverse fault and the coseismic slip is centered at much deeper (>9 km) depths compared to that of the 2020 Elazığ earthquake (~4 km).

6. Conclusions

A 19-year geodetic record (2003–2022) bracketing the January 2020, Mw 6.8 Elazığ earthquake offers unique insights into late-interseismic, coseismic and early-afterslip processes involved in the rupture of a shallow creeping fault during a major earthquake. Coseismic slip attained maximum values where previous interseismic slip had been insignificant. Conversely, coseismic slip was absent in the shallow creeping portions of the fault within 1 km of the surface, where decaying afterslip is expected to continue at decaying rates for many years. Minor slip on the surface of the fault started approximately 4.5 days after the mainshock and continued as afterslip. Large aftershocks occurred in regions of low coseismic slip, and where afterslip rates were low. Surface creep extended tens of km beyond the 40-km-long coseismic rupture. While many of these observations should come as no surprise, as they have been observed in part on strike slip fault earthquakes elsewhere, they provide a template for the future failure of creeping faults where major earthquakes are anticipated such as the Hayward (USA) (Bürgmann et al., 2000; Aagaard et al., 2012) and Chaman (Pakistan and Afghanistan) (Fattahi and Amelung, 2016) faults. In some cases, the slip distributions we observed have been modeled using theoretical assumptions concerning a range of possible behaviors. The 2020 Elazığ earthquake thus provides important geodetic constraints that may enable some of the parameters chosen in dynamic and mechanical earthquake studies to be refined, leading to more realistic scenarios of anticipated future rupture initiation and arrest, and the evolution of fault slip.

CRedit authorship contribution statement

Z. Cakir: conceptualizing the context, processing and modeling the InSAR data, and writing the manuscript. **A.M. Akoğlu:** calculating the coseismic and aftershock interferograms, and contributing to writing. **R. Bilham:** installing the creepmeter following the earthquake and contributing to writing and conceptualization.

S. Ergintav: contributing to interpretation of results. **U. Doğan, S. Özarpacı, M.H. Erkoç, A. Özdemir:** carrying out GPS campaigns and processing the data. **T. Nozadkhalil, N. Çakir:** helping with the processing of InSAR time series and correcting atmospheric delays. **C. Zabcı:** carrying out post-earthquake reconnaissance studies. **M. Basmenji, M. Köküm:** helping creepmeter installation and maintenance, and contributing to writing.

Declaration of competing interest

The authors declare that they have no known competing financial interests or personal relationships that could have appeared to influence the work reported in this paper.

Data availability

Data will be made available on request.

Acknowledgements

The SAR data are provided by ESA and JAXA (project no. P3152002). This study contains Copernicus Sentinel-1 data (2014–2021). Processing of radar images was performed at TUBITAK ULAKBIM, High Performance and Grid Computing Center (TRUBA resources). This work was supported by TÜBİTAK, Project numbers: 118Y435 and 114Y250. The creepmeter was funded by the National Science Foundation award EAR 2019910. We thank R. Harris and G. Funning for their constructive comments that greatly improved the manuscript.

Appendix A. Supplementary material

Supplementary material related to this article can be found online at <https://doi.org/10.1016/j.epsl.2023.118085>.

References

- Aagaard, B.T., Lienkaemper, J.J., Schwartz, D.P., 2012. Probabilistic estimates of surface coseismic slip and afterslip for Hayward fault earthquakes. *Bull. Seismol. Soc. Am.* 102 (3), 961–979. <https://doi.org/10.1785/0120110200>.
- Aki, K., 1979. Characterization of barriers on an earthquake fault. *J. Geophys. Res., Solid Earth* 84 (B11), 6140–6148.
- Avouac, J.P., 2015. From geodetic imaging of seismic and aseismic fault slip to dynamic modeling of the seismic cycle. *Annu. Rev. Earth Planet. Sci.* 43, 233–271.
- Bekaert, D.P.S., Walters, R.J., Wright, T.J., Hooper, A.J., Parker, D.J., 2015. Statistical comparison of InSAR tropospheric correction techniques. *Remote Sens. Environ.* 170, 40–47.
- Bilham, R., 1989. Surface slip subsequent to the 24 November 1987 Superstition Hills, California, earthquake monitored by digital creepmeters. *Bull. Seismol. Soc. Am.* 79 (2), 424–450.
- Bilham, R., 2005. Coseismic strain and the transition to surface afterslip recorded by creepmeters near the 2004 Parkfield epicenter. *Seismol. Res. Lett.* 76 (1), 49–57.
- Bletery, Q., Cavalié, O., Nocquet, J.M., Ragon, T., 2020. Distribution of interseismic coupling along the North and East Anatolian Faults inferred from InSAR and GPS data. *Geophys. Res. Lett.* 47 (16), e2020GL087775.
- Brooks, B.A., Minson, S.E., Glennie, C.L., Nevitt, J.M., Dawson, T., Rubin, R., Zaccone, D., 2017. Buried shallow fault slip from the South Napa earthquake revealed by near-field geodesy. *Sci. Adv.* 3 (7), e1700525.
- Bürgmann, R., Schmidt, D., Nadeau, R.M., d'Alessio, M., Fielding, E., Manaker, D., Murray, M.H., 2000. Earthquake potential along the northern Hayward fault, California. *Science* 289 (5482), 1178–1182.
- Cakir, Z., Ergintav, S., Özener, H., Dogan, U., Akoglu, A.M., Meghraoui, M., Reilinger, R., 2012. Onset of aseismic creep on major strike-slip faults. *Geology* 40 (12), 1115–1118.
- Carpenter, B.M., Marone, C., Saffer, D.M., 2011. Weakness of the San Andreas Fault revealed by samples from the active fault zone. *Nat. Geosci.* 4 (4), 251–254.
- Cavalié, O., Jónsson, S., 2014. Block-like plate movements in eastern Anatolia observed by InSAR. *Geophys. Res. Lett.* 41 (1), 26–31.
- Chen, K., Zhang, Z., Liang, C., Xue, C., Liu, P., 2020. Kinematics and dynamics of the 24 January 2020 Mw 6.7 Elazığ, Turkey earthquake. *Earth Space Sci.* 7 (11), e2020EA001452.
- Chen, K.H., Bürgmann, R., 2017. Creeping faults: good news, bad news? *Rev. Geophys.* 55 (2), 282–286.

- Dee, D.P., Uppala, S.M., Simmons, A.J., Berrisford, P., Poli, P., Kobayashi, S., Andrae, U., Balmaseda, M.A., Balsamo, G., Bauer, D.P., Bechtold, P., 2011. The ERA-Interim reanalysis: configuration and performance of the data assimilation system. *Q. J. R. Meteorol. Soc.* 137 (656), 553–597.
- Duman, T.Y., Emre, Ö., 2013. The East Anatolian Fault: geometry, segmentation and jog characteristics. *Geol. Soc. (Lond.) Spec. Publ.* 372 (1), 495–529.
- Emre, Ö., Duman, T.Y., Özalp, S., Şaroğlu, F., Olgun, Ş., Elmacı, H., Çan, T., 2018. Active fault database of Turkey. *Bull. Earthq. Eng.* 16 (8), 3229–3275.
- Farr, T.G., Kobrick, M., 2000. Shuttle Radar Topography Mission produces a wealth of data. *Eos* 81 (48), 583–585.
- Fattahi, H., Amelung, F., 2016. InSAR observations of strain accumulation and fault creep along the Chaman Fault system, Pakistan and Afghanistan. *Geophys. Res. Lett.* 43 (16), 8399–8406.
- Floyd, M.A., Walters, R.J., Elliott, J.R., Funning, G.J., Svarc, J.L., Murray, J.R., Hooper, A.J., Larsen, Y., Marinkovic, P., Bürgmann, R., Johanson, I.A., 2016. Spatial variations in fault friction related to lithology from rupture and afterslip of the 2014 South Napa, California, earthquake. *Geophys. Res. Lett.* 43 (13), 6808–6816.
- Funning, G.J., Parsons, B., Wright, T.J., Jackson, J.A., Fielding, E.J., 2005. Surface displacements and source parameters of the 2003 Bam (Iran) earthquake from Envisat advanced synthetic aperture radar imagery. *J. Geophys. Res., Solid Earth* 110 (B9).
- Gallovič, F., Zahradník, J., Plicka, V., Sokos, E., Evangelidis, C., Fountoulakis, I., Turhan, F., 2020. Complex rupture dynamics on an immature fault during the 2020 Mw 6.8 Elazığ earthquake, Turkey. *Commun. Earth Environ.* 1 (1), 1–8.
- Harris, R.A., 2017. Large earthquakes and creeping faults. *Rev. Geophys.* 55 (1), 169–198.
- Herring, T.A., King, R.W., McClusky, S.C., 2010. Introduction to Gamit/Globk. Massachusetts Institute of Technology, Cambridge, Massachusetts.
- Hooper, A., Bekaert, D., Spaans, K., Arikan, M., 2012. Recent advances in SAR interferometry time series analysis for measuring crustal deformation. *Tectonophysics* 514, 1–13.
- Hough, S.E., Martin, S.S., 2015. The 1868 Hayward fault, California, earthquake: implications for earthquake scaling relations on partially creeping faults. *Bull. Seismol. Soc. Am.* 105 (6), 2894–2909.
- Hsu, Y.J., Simons, M., Avouac, J.P., Galetzka, J., Sieh, K., Chlieh, M., Bock, Y., 2006. Frictional afterslip following the 2005 Nias-Simeulue earthquake, Sumatra. *Science* 312 (5782), 1921–1926.
- Johanson, I.A., Fielding, E.J., Rolandone, F., Bürgmann, R., 2006. Coseismic and post-seismic slip of the 2004 Parkfield earthquake from space-geodetic data. *Bull. Seismol. Soc. Am.* 96 (4B), S269–S282. <https://doi.org/10.1785/0120050818>.
- Jónsson, S., Zebker, H., Segall, P., Amelung, F., 2002. Fault slip distribution of the 1999 M w 7.1 Hector Mine, California, earthquake, estimated from satellite radar and GPS measurements. *Bull. Seismol. Soc. Am.* 92 (4), 1377–1389.
- Kampes, B., Usai, S., 1999. Doris: The delft object-oriented radar interferometric software. In: Proceedings of the 2nd International Symposium on Operationalization of Remote Sensing. Enschede, The Netherlands, vol. 1620.
- Kaneko, Y., Avouac, J.P., Lapusta, N., 2010. Towards inferring earthquake patterns from geodetic observations of interseismic coupling. *Nat. Geosci.* 3 (5), 363–369.
- Konca, A.Ö., Karabulut, H., Güvercin, S.E., Eskiköy, F., Özarpaç, S., Özdemir, A., Doğan, U., 2021. From interseismic deformation with near-repeating earthquakes to coseismic rupture: a unified view of the 2020 Mw 6.8 Sivrice (Elazığ) Eastern Turkey earthquake. *J. Geophys. Res., Solid Earth* 126 (10), e2021JB021830.
- Liang, C., Fielding, E.J., 2017. Measuring azimuth deformation with L-band ALOS-2 ScanSAR interferometry. *IEEE Trans. Geosci. Remote Sens.* 55 (5), 2725–2738.
- Lindh, A.G., Boore, D.M., 1981. Control of rupture by fault geometry during the 1966 Parkfield earthquake. *Bull. Seismol. Soc. Am.* 71 (1), 95–116.
- Maerten, F., Resor, P., Pollard, D., Maerten, L., 2005. Inverting for slip on three-dimensional fault surfaces using angular dislocations. *Bull. Seismol. Soc. Am.* 95 (5), 1654–1665.
- Marone, C.J., Scholtz, C.H., Bilham, R., 1991. On the mechanics of earthquake afterslip. *J. Geophys. Res., Solid Earth* 96 (B5), 8441–8452.
- Melgar, D., Ganas, A., Taymaz, T., Valkaniotis, S., Crowell, B.W., Kapetanidis, V., Öcalan, T., 2020. Rupture kinematics of 2020 January 24 Mw 6.7 Doğanlıoğlu-Sivrice, Turkey earthquake on the East Anatolian Fault Zone imaged by space geodesy. *Geophys. J. Int.* 223 (2), 862–874.
- Nevitt, J.M., Brooks, B.A., Catchings, R.D., Goldman, M.R., Ericksen, T.L., Glennie, C.L., 2020. Mechanics of near-field deformation during co- and post-seismic shallow fault slip. *Sci. Rep.* 10 (1), 5031. <https://doi.org/10.1038/s41598-020-61400-9>.
- Nissen, E., Elliott, J.R., Sloan, R.A., Craig, T.J., Funning, G.J., Hutko, A., Wright, T.J., 2016. Limitations of rupture forecasting exposed by instantaneously triggered earthquake doublet. *Nat. Geosci.* 9 (4), 330–336.
- Noda, H., Lapusta, N., 2013. Stable creeping fault segments can become destructive as a result of dynamic weakening. *Nature* 493 (7433), 518–521.
- Parker, J., Donnellan, A., Bilham, R., Grant Ludwig, L., Pierce, M., Wang, J., Mowery, N., 2021. Buried aseismic slip and off-fault deformation on the southernmost San Andreas Fault triggered by the 2010 El Mayor Cucapah earthquake revealed by UAVSAR. <https://doi.org/10.1029/2021EA001682>.
- Pousse-Beltran, L., Nissen, E., Bergman, E.A., Cambaz, M.D., Gaudreau, É., Karasözen, E., Tan, F., 2020. The 2020 Mw 6.8 Elazığ (Turkey) earthquake reveals rupture behavior of the East Anatolian Fault. *Geophys. Res. Lett.* 47 (13), e2020GL088136.
- Ragon, T., Simons, M., Bletery, Q., Cavalie, O., Fielding, E., 2021. A stochastic view of the 2020 Elazığ Mw 6.8 earthquake (Turkey). *Geophys. Res. Lett.* 48 (3), e2020GL090704.
- Reilinger, R., McClusky, S., Vernant, P., Lawrence, S., Ergintav, S., Cakmak, R., Karam, G., 2006. GPS constraints on continental deformation in the Africa-Arabia-Eurasia continental collision zone and implications for the dynamics of plate interactions. *J. Geophys. Res., Solid Earth* 111 (B5).
- Rosen, P.A., Gurrola, E.M., Agram, P.S., Sacco, G.F., Lavalle, M., 2015. The InSAR Scientific Computing Environment (ISCE): a Python framework for Earth science. In: AGU Fall Meeting Abstracts, vol. 2015, IN11C-1789.
- Rosen, P.A., Hensley, S., Joughin, I.R., Li, F.K., Madsen, S.N., Rodriguez, E., Goldstein, R.M., 2000. Synthetic aperture radar interferometry. *Proc. IEEE* 88 (3), 333–382.
- Sandwell, D., Mellors, R., Tong, X., Wei, M., Wessel, P., 2011. Open radar interferometry software for mapping surface deformation.
- Şengör, A.M.C., Görür, N., Şaroğlu, F., 1985. Strike-slip faulting and related basin formation in zones of tectonic escape: Turkey as a case study. In: Biddle, Kevin T., Christie-Blick, Nicholas (Eds.), Strike-Slip Deformation, Basin Formation, and Sedimentation. In: Society of Economic Paleontologists and Mineralogists Special Publications, vol. 37, pp. 227–264.
- Sieh, K.E., 1978. Slip along the San Andreas fault associated with the great 1857 earthquake. *Bull. Seismol. Soc. Am.* 68 (5), 1421–1448.
- Sudhaus, H., Jónsson, J., 2009. Improved source modelling through combined use of InSAR and GPS under consideration of correlated data errors: application to the June 2000 Kleifarvatn earthquake, Iceland. *Geophys. J. Int.* 176 (2), 389–404.
- Tatar, O., Sözbilir, H., Koçbulut, F., Bozkurt, E., Aksoy, E., Eski, S., Metin, Y., 2020. Surface deformations of 24 January 2020 Sivrice (Elazığ)-Doğanlıoğlu (Malatya) earthquake (Mw = 6.8) along the Pütürge segment of the East Anatolian Fault Zone and its comparison with Turkey's 100-year-surface ruptures. *Mediterr. Geosci. Rev.* 2 (3), 385–410.
- Taymaz, T., Ganas, A., Yolsal-Çevikbilen, S., Vera, F., Eken, T., Erman, C., Öcalan, T., 2021. Source mechanism and rupture process of the 24 January 2020 Mw 6.7 Doğanlıoğlu-Sivrice earthquake obtained from seismological waveform analysis and space geodetic observations on the East Anatolian Fault Zone (Turkey). *Tectonophysics* 804, 228745.
- Thatcher, W., 1975. Strain accumulation and release mechanism of the 1906 San Francisco earthquake. *J. Geophys. Res.* 80 (35), 4862–4872.
- Thomas, A.L., 1993. POLU3D: a three-dimensional, polygonal element, displacement discontinuity boundary element computer program with applications to fractures, faults, and cavities in the earth's crust. Master Thesis. Stanford University.
- Thomas, M.Y., Avouac, J.P., Champenois, J., Lee, J.C., Kuo, L.C., 2014. Spatiotemporal evolution of seismic and aseismic slip on the Longitudinal Valley Fault, Taiwan. *J. Geophys. Res., Solid Earth* 119 (6), 5114–5139.
- Wells, D.L., Coppersmith, K.J., 1994. New empirical relationships among magnitude, rupture length, rupture width, rupture area, and surface displacement. *Bull. Seismol. Soc. Am.* 84 (4), 974–1002.